npj | parkinson's disease

Article

Published in partnership with the Parkinson's Foundation

https://doi.org/10.1038/s41531-024-00748-5

Adult-onset deletion of *ATP13A2* in mice induces progressive nigrostriatal pathway dopaminergic degeneration and lysosomal abnormalities

Madalynn L. Erb[1,2], Kayla Sipple[1], Nathan Levine[1], Xi Chen[1] & Darren J. Moore[1,2]

Although most cases of Parkinson's disease (PD) are sporadic, mutations in over 20 genes are known to cause heritable forms of the disease. Recessive loss-of-function mutations in *ATP13A2*, a lysosomal transmembrane $P5_B$-type ATPase and polyamine exporter, can cause early-onset familial PD. Familial *ATP13A2* mutations are also linked to related neurodegenerative diseases, including Kufor-Rakeb syndrome, hereditary spastic paraplegias, neuronal ceroid lipofuscinosis, and amyotrophic lateral sclerosis. Despite the severe effects of *ATP13A2* mutations in humans, *ATP13A2* knockout (KO) mice fail to exhibit neurodegeneration even at advanced ages, making it challenging to study the neuropathological effects of ATP13A2 loss in vivo. Germline deletion of *ATP13A2* in rodents may trigger the upregulation of compensatory pathways during embryonic development that mask the full neurotoxic effects of ATP13A2 loss in the brain. To explore this idea, we selectively deleted *ATP13A2* in the adult mouse brain by the unilateral delivery of an AAV-Cre vector into the substantia nigra of young adult mice carrying conditional *lox*P-flanked *ATP13A2* KO alleles. We observe a progressive loss of striatal dopaminergic nerve terminals at 3 and 10 months after AAV-Cre delivery. Cre-injected mice also exhibit robust dopaminergic neuronal degeneration in the substantia nigra at 10 months. Adult-onset *ATP13A2* KO also recreates many of the phenotypes observed in aged germline *ATP13A2* KO mice, including lysosomal abnormalities, p62-positive inclusions, and neuroinflammation. Our study demonstrates that the adult-onset homozygous deletion of *ATP13A2* in the nigrostriatal pathway produces robust and progressive dopaminergic neurodegeneration that serves as a useful in vivo model of *ATP13A2*-related neurodegenerative diseases.

Parkinson's disease (PD) is the most common neurodegenerative movement disorder. PD is characterized by the progressive and irreversible loss of dopaminergic neurons in the substantia nigra pars compacta (SNpc) resulting in a variety of motor symptoms, including resting tremor, rigidity, bradykinesia, and postural instability. Most cases of PD are sporadic and of unknown cause. Risk for developing sporadic PD is thought to result from a combination of genetic and environmental factors together with aging. Interestingly, 5-10% of PD cases are familial and are known to be linked to inherited mutations in single genes i.e. monogenic PD[1,2].

At this time, mutations in 21 genes have been identified as the cause of familial forms of PD[3]. These genes offer insights into putative molecular disease pathways and provide opportunities to develop animal models that recreate the progressive neuropathology and degeneration in the nigrostriatal pathway that characterizes PD. A surprising number of familial PD genes are involved in intracellular trafficking and protein degradation, implicating these pathways in PD pathogenesis[4,5]. Homozygous loss-of-function mutations in *ATP13A2* (*PARK9*) cause autosomal recessive, juvenile-onset atypical parkinsonism whereas heterozygous mutations in *ATP13A2* have also been linked to early-onset familial PD[6–8]. *ATP13A2* mutations have also been linked to other familial neurodegenerative diseases, including Kufor-Rakeb syndrome (KRS), hereditary spastic paraplegias (HSPs), amyotrophic lateral sclerosis (ALS), neurodegeneration with

[1]Department of Neurodegenerative Science, Van Andel Institute, Grand Rapids, MI, USA. [2]Aligning Science Across Parkinson's (ASAP) Collaborative Research Network, Chevy Chase, MD, USA. e-mail: darren.moore@vai.org

brain iron accumulation (NBIA) and neuronal ceroid lipofuscinosis (NCL)[9–14].

ATP13A2 is a lysosomal transmembrane $P5_B$-type ATPase that can function as a polyamine transporter[15–19]. ATP13A2 uses ATP hydrolysis to preferentially pump spermine and spermidine from the lumen of late endosomes and lysosomes into the cytosol, thereby regulating polyamine homeostasis in cells[15]. *ATP13A2* disease-linked mutations or depletion of ATP13A2 protein is known to disrupt lysosomal function in cells, causing the accumulation of lysosomes, lysosomal swelling, reduced lysosomal acidity and decreased lysosomal degradative capacity[20,21]. ATP13A2 mRNA and protein are widely expressed throughout the mammalian brain in multiple cell types. Notably, changes in ATP13A2 mRNA and protein levels have been observed in the SNpc and other brain regions of subjects with sporadic PD or dementia with Lewy bodies (DLB)[18,22,23]. These findings suggest that ATP13A2 may be a promising therapeutic target for treating sporadic PD. Decreases in ATP13A2 expression could contribute to disease pathogenesis or progression, while increases in expression may be a compensatory mechanism to counteract ongoing neuropathological cellular and molecular changes.

Despite the severe and early-onset impact of *ATP13A2* mutations in humans, germline *ATP13A2* knockout (KO) mice do not exhibit dopaminergic neurodegeneration in the nigrostriatal pathway or noticeable atrophy in other brain regions, even with advanced age[24,25]. Aged germline *ATP13A2* KO mice experience modest motor impairment as well as reactive astrogliosis throughout the brain[24,25]. Additionally, *ATP13A2* KO mice show signs of impaired lysosomal and autophagic function in the brain that become more severe with age, including the accumulation of lysosomal proteins LAMP1 and LAMP2, the accumulation of lipofuscin and ubiquitin aggregation[24,25].

The discrepancy between human subjects and rodent models bearing homozygous *ATP13A2* mutations or deletions makes it challenging to study the neuropathological effects of ATP13A2 loss in vivo. We hypothesize that germline deletion of *ATP13A2* in rodents may trigger the upregulation of compensatory pathways during embryonic development that mask the full neurotoxic effects of *ATP13A2* KO in the brain. Depleting ATP13A2 protein from the mature adult brain, which is likely less resilient and plastic to disruptions in critical molecular pathways, could potentially recreate neurotoxic effects similar to those observed in human subjects. To deplete ATP13A2 in the nigrostriatal pathway of adult mice, we unilaterally delivered AAV-Cre vectors to the SNpc of young adult mice bearing conditional *lox*P-flanked *ATP13A2* KO alleles. Conditional KO mice were assessed at 3 or 10 months after Cre recombinase delivery to monitor the genomic KO of *ATP13A2*, dopaminergic neurodegeneration, axonal degeneration, pathological protein aggregation, neuroinflammation and lysosomal abnormalities.

Results

Conditional deletion of *ATP13A2* in the substantia nigra of adult mice

To selectively delete *ATP13A2* in the nigrostriatal pathway of adult mice, homozygous *ATP13A2* floxed KO mice (Fig. 1a) (age 2–6 months) were subjected to unilateral stereotactic injection of either recombinant AAV2/5-Cre-GFP (AAV-Cre) vector, or AAV2/5-GFP (AAV-GFP) vector as a control, directly into the SNpc (Fig. 1b). Using immunofluorescence for GFP, we find that Cre-GFP or GFP are detectable throughout the ipsilateral ventral midbrain at both 3 and 10 months after AAV injection compared to the contralateral non-injected hemisphere (Fig. 1c). Cre-GFP protein is abundant at both timepoints and, as expected, is largely nuclear due to the presence of a nuclear localization signal. GFP protein alone exhibits a more diffuse subcellular localization and is also detected at 3 and 10 months. The GFP fluorescence signal in mice injected with AAV-GFP is moderately less abundant than that in AAV-Cre-GFP mice, which may result from its reduced stability in the cytoplasmic compartment.

ATP13A2 floxed KO mice contain *lox*P sites flanking exons 2 and 3 (Fig. 1a)[24]. Cre-mediated recombination results in the removal of exons 2 and 3 from *ATP13A2* and the introduction of a premature stop codon in exon 4[24]. To confirm the efficiency of genomic recombination at the *ATP13A2* locus in mice, we extracted genomic DNA from ventral midbrain tissues 3 months after injection of AAV-Cre or AAV-GFP and performed genomic PCR to detect floxed and KO alleles. We detect the *ATP13A2* KO allele exclusively in the ipsilateral ventral midbrain of mice injected with AAV-Cre, compared to the contralateral midbrain (Fig. 1d). The floxed allele is detected in both the contralateral and ipsilateral ventral midbrain of mice injected with AAV-GFP as well as in AAV-Cre mice, as expected (Fig. 1d). To further confirm successful *ATP13A2* KO, we performed BaseScope™ in situ hybridization using a custom probe designed to recognize exons 2–3 of the ATP13A2 mRNA transcript (Fig. 1e and Supplementary Fig. 1). At 3 months post-injection with AAV-GFP, mice express ATP13A2 mRNA equivalently throughout the dorsal midbrain and the SN in both ipsilateral and contralateral hemispheres. AAV-Cre-injected mice have similarly high levels of ATP13A2 mRNA in the contralateral SN yet exhibit a robust reduction in ATP13A2 mRNA BaseScope™ signal in the ipsilateral SN (Fig. 1e and Supplementary Fig. 1). Quantitation of BaseScope™ area for ATP13A2 mRNA signal reveals significantly reduced levels of ATP13A2 mRNA only in the ipsilateral SN of AAV-Cre-injected mice. To examine ATP13A2 mRNA expression specifically in dopaminergic neurons in the SNpc, we used TH immunolabeling combined with ATP13A2 BaseScope™ in situ hybridization 3 months after AAV-Cre injections. We find ATP13A2 mRNA expression in TH-positive neurons in the contralateral SNpc but its absence in ipsilateral SNpc TH-positive neurons (Fig. 1f). Of interest, we also observe a marked increase of ATP13A2 mRNA signal in some cells at the periphery of the ipsilateral ventral midbrain region in AAV-Cre-injected mice, but not with AAV-GFP (Supplementary Fig. 1), which we hypothesize may be due to a compensatory upregulation of ATP13A2 in select WT neurons or glial cells in response to proximal *ATP13A2* KO.

Since the AAV2/5 vectors utilized in this study contain ubiquitous, constitutive CMV promoters, it is important to evaluate which cell types express Cre-GFP and subsequently knockout ATP13A2 expression. For this purpose, we analyzed the co-expression of Cre-GFP with TH, parvalbumin, Iba1 or GFAP in the ipsilateral SN of AAV-Cre-injected mice. We find that Cre-GFP is largely restricted to tyrosine hydroxylase (TH; ~65%)- or parvalbumin (~ 87%)-positive neurons with little to no expression in Iba1-positive microglia or GFAP-positive astrocytes (Fig. 1g). We also observe a strong overlap between NeuN-positive neurons and Cre-GFP-expressing cells, with nearly all Cre-GFP expression occurring in NeuN-positive neurons (Supplementary Fig. 2). Together, these data indicate robust and prolonged expression of GFP and Cre-GFP that is restricted to neurons in the ipsilateral ventral midbrain, with Cre expression inducing efficient genomic recombination and subsequent depletion of ATP13A2 mRNA from the ipsilateral SN.

ATP13A2 KO induces progressive nigrostriatal pathway dopaminergic neurodegeneration

We next examined dopaminergic neurons in the nigrostriatal pathway 3 or 10 months after AAV-GFP or AAV-Cre injections. Dopaminergic neurons in the SNpc express TH and project their axons to medium-sized spiny neurons in the striatum. To first evaluate these axonal projections in the striatum, coronal brain sections were immunostained for TH and optical density was measured comparing the ipsilateral and contralateral striata. After 3 months, we find a significant loss (29.05 ± 6.19%) of TH-positive dopaminergic nerve terminals in the ipsilateral striatum of AAV-Cre-injected mice relative to the contralateral striatum, with no obvious terminal loss (5.27 ± 5.42%) in AAV-GFP-injected mice (Fig. 2a). However, in the SNpc at 3 months, we do not find a significant loss of TH-positive dopaminergic (12.67 ± 7.81%) or total Nissl-positive (9.22 ± 7.49%) neurons in mice injected with AAV-Cre (Fig. 2b), suggesting that early axonal degeneration in the nigrostriatal pathway occurs prior to obvious nigral dopaminergic neuronal loss.

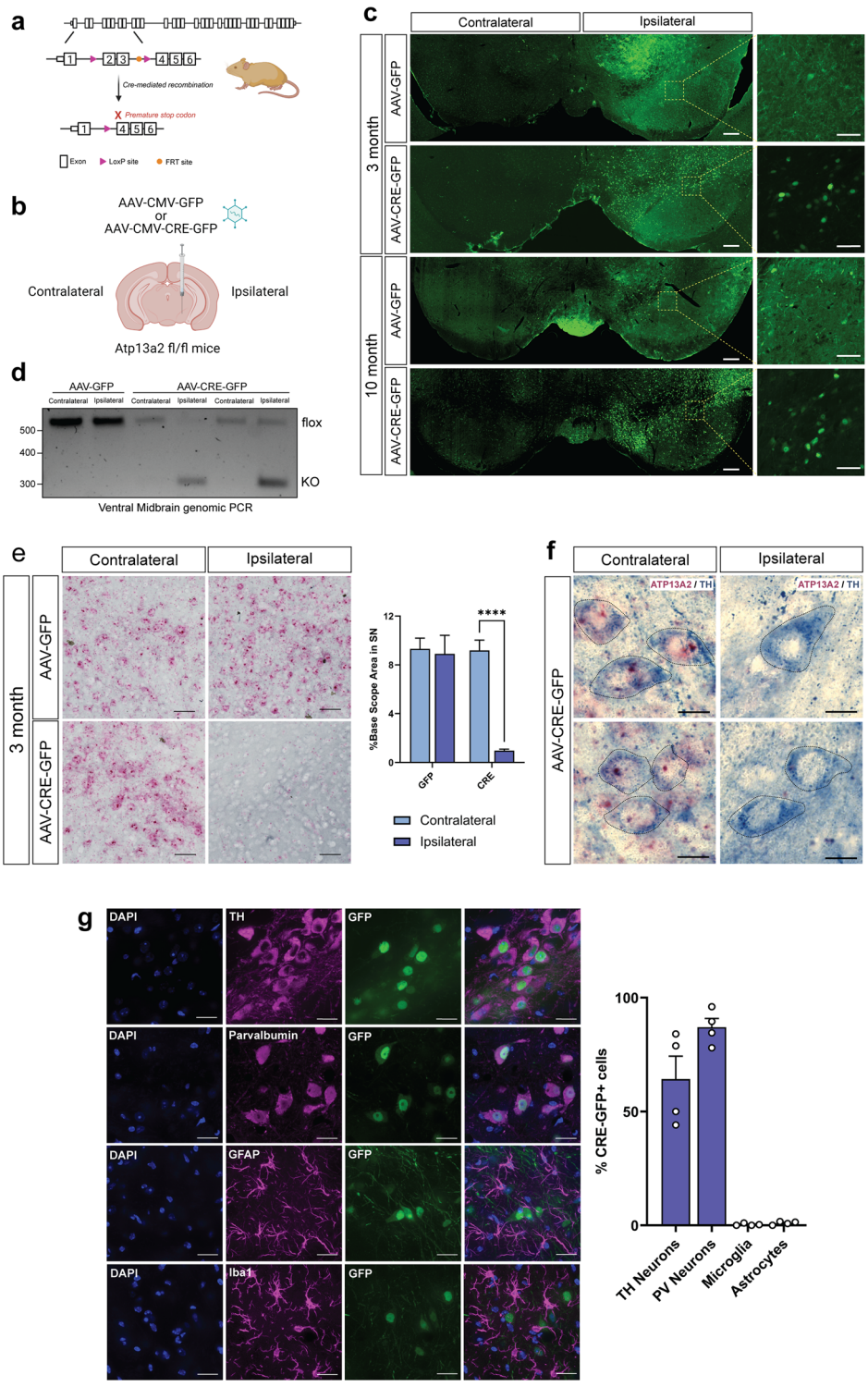

Fig. 1 | *ATP13A2* knockout in adult mice through unilateral injection of AAV-Cre into the substantia nigra. a Position of *lox*P sites and *FRT* sites in *ATP13A2* floxed KO mice. Cre-mediated recombination results in removal of exons 2 and 3 and formation of a premature stop codon in exon 4. **b** Unilateral injection of recombinant AAV-CMV-Cre-GFP or control AAV-CMV-GFP vectors into the SN in young adult mice. **c** GFP or Cre-GFP immunofluorescence in the ipsilateral and contralateral ventral midbrain at 3 or 10 months after AAV delivery. High magnification images of GFP or Cre-GFP are shown taken from the boxed region, as indicated. Scale bars: 200 µm or 50 µm. **d** Genomic PCR in ventral midbrain tissue of floxed KO mice expressing Cre-GFP or GFP amplifying *ATP13A2* flox and KO alleles using primers flanking exons 2-3. **e** BaseScope™ in situ hybridization to detect *ATP13A2* mRNA transcript (red puncta) in the ventral midbrain at 3 months. Scale bars: 50 µm. Percent BaseScope™-positive area in the SN was measured using HALO analysis software. Bars represent mean ± SEM, $n = 4$ animals per group. $^{****}P < 0.0001$ by two-way ANOVA with Sidak's multiple comparisons test. **f** Representative images of ATP13A2 BaseScope™ in situ hybridization (red) combined with TH immunostaining (blue, outlined) in the SNpc of AAV-Cre-injected mice at 3 months. Scale bars: 10 µm. **g** Cre-GFP immunofluorescence combined with TH, parvalbumin, GFAP or Iba1 immunofluorescence in the ipsilateral SN of AAV-Cre-injected mice at 3 months. Scale bars: 20 µm. Data are expressed as the percent of each cell population in the SN that is transduced with Cre-GFP, with ~65% TH-positive neurons and ~87% parvalbumin-positive neurons expressing Cre-GFP. Bars represent mean ± SEM, $n = 4$ animals per group.

At 10 months post-injection, we observe a more robust loss of TH-positive nerve terminals (47.67 ± 5.16%) in the ipsilateral striatum of AAV-Cre-injected mice (Fig. 2c), as well as a significant loss of TH-positive dopaminergic (34.68 ± 4.99%) and Nissl-positive neurons (33.29 ± 4.97%) in the ipsilateral SNpc relative to the contralateral hemisphere (Fig. 2d). The parallel loss of Nissl-positive neurons confirms neuronal degeneration rather than a loss of TH phenotype. Mice injected with AAV-GFP fail to exhibit any loss of dopaminergic neurons (4.85 ± 7.31%) or their terminals (-20.10 ± 15.93%) at 10 months (Fig. 2c, d). These data indicate the progressive degeneration of the nigrostriatal pathway that worsens from 3 to 10 months in the AAV-Cre-injected mice. We also note a qualitative loss of TH-positive dopaminergic neurons (A10 population) in the ipsilateral ventral tegmental area (VTA) of AAV-Cre-injected mice at 10 months (Fig. 2d), however, we focused our stereological analysis on SNpc neurons. To determine whether neurodegeneration induced by ATP13A2 depletion is selective to dopaminergic neurons or is non-specific, we immunostained and quantified parvalbumin-positive and GAD67-positive neurons that represent two additional neuronal subpopulations in the substantia nigra (Supplementary Fig. 3). We find no difference in the number of parvalbumin-positive neurons in the ipsilateral SN of mice injected with AAV-Cre or

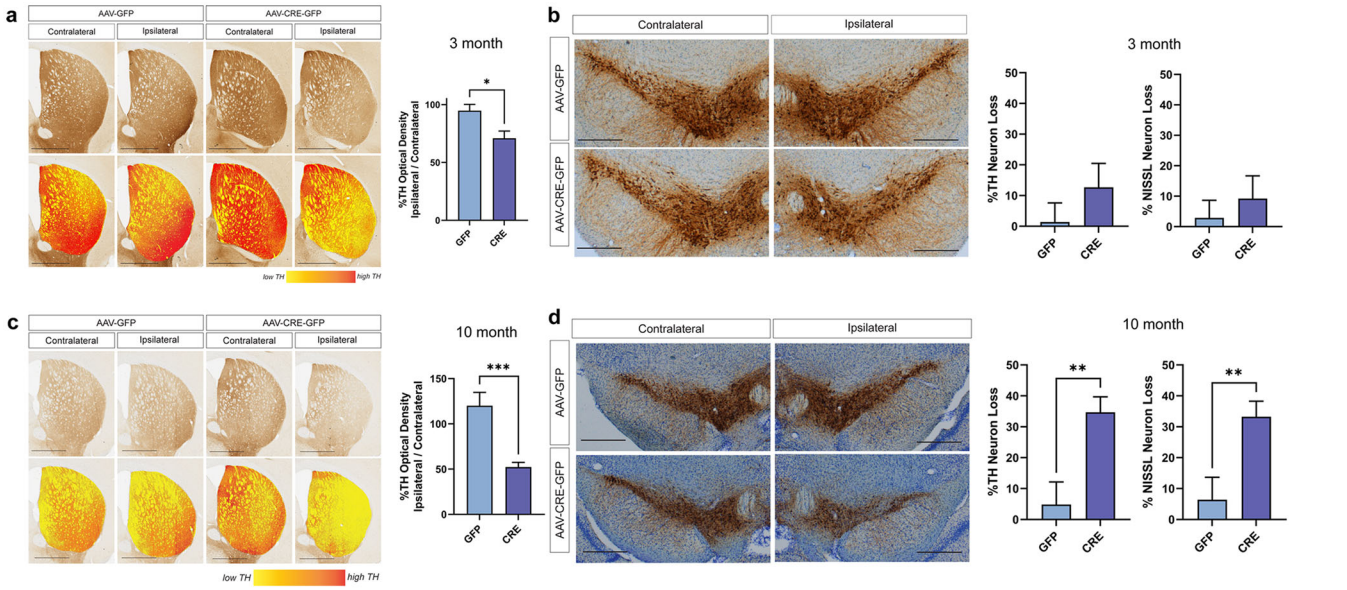

Fig. 2 | *ATP13A2* knockout causes progressive degeneration of the nigrostriatal dopaminergic pathway over 10 months. a Representative images of TH immunostaining in the striatum of *ATP13A2* floxed KO mice injected with AAV-GFP or AAV-Cre vectors at 3 months. Scale bars: 1 mm. Striatal TH optical density was measured using HALO analysis software with data expressed as % TH optical density of the ipsilateral striatum versus the contralateral striatum. Bars represent mean ± SEM, $n = 7$-8 mice per group. $^{*}P < 0.05$ by unpaired, Student's *t*-test. **b** Representative images of TH immunostaining in the SN at 3 months. Scale bars: 400 µm. Unbiased stereological analysis of TH+ and Nissl+ neurons in the SNpc at 3 months with data expressed as % TH+ or Nissl+ neuron loss versus the contralateral SNpc. Bars represent mean ± SEM, $n = 9$–10 mice per group. **c** Images of striatal TH immunostaining and striatal TH optical density in mice at 10 months after AAV delivery. Scale bars: 1 mm. Bars represent mean ± SEM, $n = 13$-14 mice per group. $^{***}P < 0.001$ by unpaired, Student's *t*-test. **d** Images of SN TH immunostaining and stereological counts of nigral TH+ and Nissl+ neurons at 10 months. Scale bars: 400 µm. Bars represent mean ± SEM, $n = 12$ mice per group. $^{**}P < 0.01$ by unpaired, Student's *t*-test.

AAV-GFP, relative to the contralateral SN (Supplementary Fig. 3). Similarly, there is no change in the mean fluorescence intensity of the GAD67-positive neuropil immunostaining in the ipsilateral SN of AAV-Cre or AAV-GFP-injected mice (Supplementary Fig. 3). These data suggest that dopaminergic neurons in the ventral midbrain are selectively vulnerable to the neurotoxic effects of ATP13A2 depletion relative to other neuronal subtypes.

One possibility in *ATP13A2* floxed KO mice is that the sustained expression of Cre-GFP in the ventral midbrain over 10 months could independently induce toxicity in nigral dopaminergic neurons. Since our experimental strategy employed homozygous *ATP13A2* floxed KO mice without producing WT littermate controls, we instead used an alternative cohort of mice on a similar C57BL/6 J genetic background. As such, in establishing suitable AAV-Cre titers, we had previously conducted independent experiments by delivering the same titer of AAV-Cre-GFP vector into the unilateral SNpc of a different mouse model, homozygous ROSA26-LRRK2^{R1441C} conditional transgenic mice, that induces Cre-dependent human R1441C LRRK2 expression (Supplementary Fig. 4). These R1441C LRRK2 mice do not normally develop dopaminergic neuronal loss following Cre-mediated recombination using dopamine transporter (DAT)-Cre even with prolonged aging up to 24 months[26]. While we observe sustained Cre-GFP expression in the ipsilateral SNpc of R1441C-LRRK2 mice at 12 months after AAV-Cre delivery, we do not observe any quantitative loss of striatal TH-positive nerve terminals or nigral dopaminergic neurons relative to the non-injected contralateral hemisphere (Supplementary Fig. 4). These data clearly demonstrate that Cre-GFP expression alone using this titer of AAV2/5 vector (i.e. 1×10^{10} vg) is generally well tolerated and is not sufficient to induce neurotoxic effects within the nigrostriatal pathway over these prolonged time periods.

ATP13A2 depletion induces transient neuroinflammation in the substantia nigra

Germline *ATP13A2* KO mice exhibit reactive astrogliosis as early as 1 month of age, which becomes progressively more severe up to 12–18 months[24]. To examine neuroinflammation in *ATP13A2* floxed KO mice injected with AAV-Cre or AAV-GFP, midbrain sections were immunostained for the astrocyte marker, GFAP, and the microglial marker, Iba1. At 3 months, we find increased GFAP-positive immunolabeling in the ipsilateral SN of both AAV-Cre and AAV-GFP-injected mice relative to the contralateral SN (Fig. 3a). Notably, we observe a significantly larger increase in GFAP signal in the ipsilateral SN with AAV-Cre compared to AAV-GFP. At 10 months, there remains a modest yet significant increase in GFAP signal in the ipsilateral SN of AAV-Cre-injected mice but no change in AAV-GFP mice (Fig. 3a). Increases in GFAP-positive immunolabeling in this KO model appear to result from a combination of AAV-related inflammation and the response to ATP13A2 depletion. Unlike germline *ATP13A2* KO mice, we do not observe progressive astrogliosis as the mice age. Instead, reactive astrogliosis appears to be somewhat transient and is largely attenuated 10 months after AAV-Cre injection.

To evaluate microglial activation in these mice, we immunostained midbrain sections for Iba1 and quantified microglial number and morphology (Fig. 3b). Microglial activation is characterized by (1) microglial recruitment to the site of neuronal injury, resulting in increased microglial density, and (2) transformation from a resting ramified morphology to an activated ameboid morphology. At 3 months, AAV-GFP-injected mice show no change in Iba1-positive total area, microglial density or microglial cell body area in the ipsilateral SN (Fig. 3b), suggesting the absence of microglial activation. AAV-Cre-injected mice exhibit a significant increase in Iba1-positive area, microglial density and cell body area, in the ipsilateral SN relative to the contralateral SN. Although this microglial activation is relatively modest, it appears to be specific to ATP13A2 depletion, as it does not occur with AAV-GFP injection. Similar to the reactive astrogliosis in these mice, microglial activation is also largely attenuated by 10 months after AAV-Cre delivery (Fig. 3b). Therefore, microglial activation also occurs in a transient and early manner.

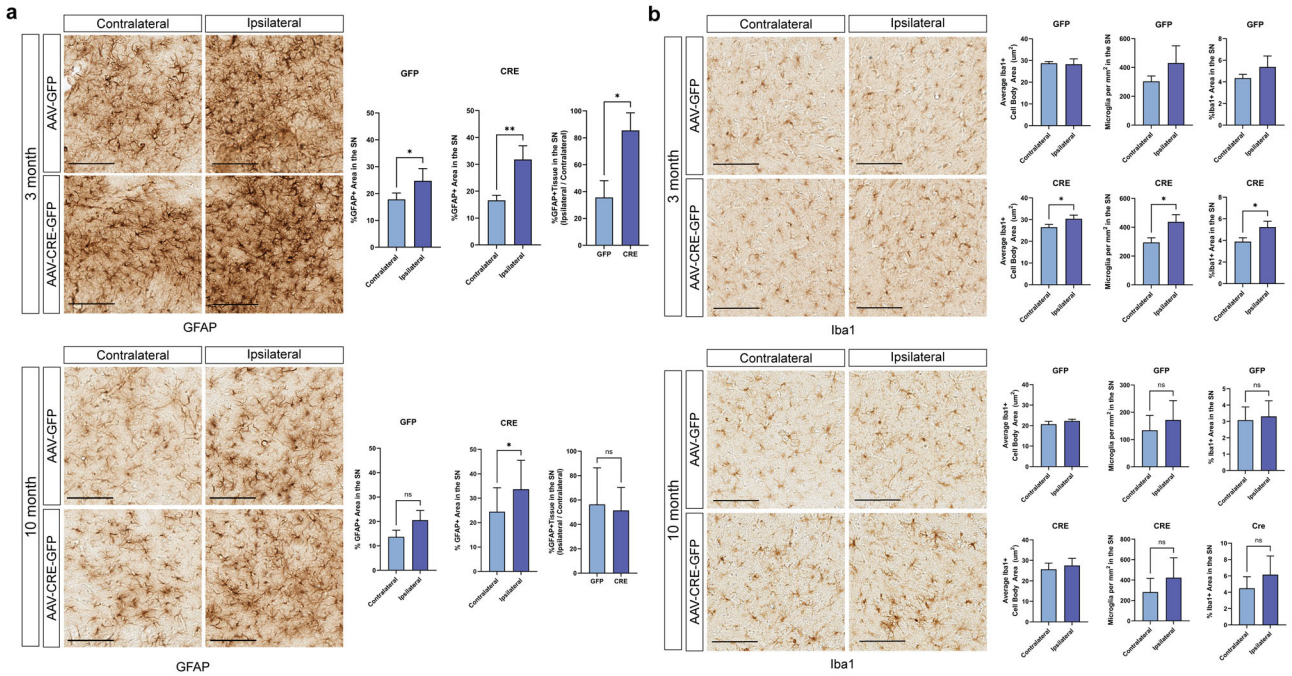

Fig. 3 | *ATP13A2* KO induces transient neuroinflammation in the ventral midbrain. a Representative images of GFAP immunostaining in the SN of *ATP13A2* floxed KO mice unilaterally injected with AAV-GFP or AAV-Cre-GFP vectors at 3 or 10 months. Scale bars: 100 µm. GFAP-positive area was measured in the ipsilateral versus contralateral hemisphere of GFP or Cre-expressing mice using HALO analysis software. Bars represent mean ± SEM, $n = 8$ (at 3 months) or $n = 4$ (at 10 months) mice per group. $^*P < 0.05$ or $^{**}P < 0.01$ by paired Student's *t*-test (% GFAP-positive area) or unpaired Student's *t*-test (% GFAP-positive area, Ipsilateral / Contralateral). **b** Representative images of Iba1 immunostaining in the SN of *ATP13A2* floxed KO mice at 3 or 10 months. Scale bars: 100 µm. Iba1-positive microglial number per mm^2, percent Iba1+ area, or cell body area (µm^2) was measured in the ipsilateral versus contralateral SN of GFP or Cre-expressing mice using HALO analysis software at 3 or 10 months. Bars represent mean ± SEM, $n = 4$ mice per group. $^*P < 0.05$ by paired Student's *t*-test. *ns*, not significant.

Lack of axonal degeneration and protein aggregation in *ATP13A2* KO mice

Given the progressive nigrostriatal dopaminergic pathway degeneration occurring over 10 months in AAV-Cre-injected mice, we evaluated whether axonal damage or degeneration also occurs in these brain regions. Gallyas silver staining was used to label degenerating axons in the striatum or SN (Fig. 4a). Surprisingly, we do not detect silver-positive degenerating neurites (black fibers) in the ipsilateral striatum or SN of AAV-Cre or AAV-GFP-injected mice at 3 or 10 months (Fig. 4a). Given the relatively slow progression of TH-positive nerve terminal and cell body degeneration, it is possible that degenerating axons or dendrites are removed from the brain as degeneration occurs, making them challenging to detect.

We next evaluated whether pathological protein aggregation occurs in the conditional *ATP13A2* KO mice. At 10 months, we do not observe the accumulation of pSer129-α-synuclein, a marker of Lewy body pathology, or pSer202/pThr205-tau (AT8), a marker of neurofibrillary tangle pathology, in the ventral midbrain of AAV-Cre-injected mice (Fig. 4b, c). We also find no change in the optical density of total α-synuclein immunostaining, or evidence of α-synuclein aggregation or altered distribution, in the ipsilateral SN of AAV-Cre-injected mice (Fig. 4d). These findings are consistent with a previous report that 18-month-old germline *ATP13A2* KO mice do not exhibit increased levels of pSer129-α-synuclein in cortical lysates[24]. Aged germline *ATP13A2* KO mice are reported to exhibit a modest increase in the levels of SDS-soluble α-synuclein in the hippocampus, however, this has not been observed in all *ATP13A2* KO mouse lines and was not observed in the cortex, striatum, midbrain or cerebellum[24,25]. Total tau and huntingtin protein levels are also unchanged in aged germline *ATP13A2* KO mice[25]. At this time, neuropathology has only been reported in one human subject with *ATP13A2*-linked neurodegenerative disease[27]. Interestingly, Chien et al. report no aggregation of α-synuclein, pSer202/pThr205-tau (AT8), β-amyloid, TDP43 or p62, in brain tissue from a KRS subject, potentially suggesting that *ATP13A2*-related neuropathology may not involve protein aggregation[27].

Lysosomal Abnormalities in *ATP13A2* KO mice

Germline *ATP13A2* KO mice develop pronounced age-dependent lysosomal pathology throughout the brain[24,25]. This lysosomal pathology consists of the accumulation of lysosomal proteins and lipofuscin as well as aggregation of the autophagy proteins ubiquitin and p62/SQSTM1[24,25]. At 10 months after AAV-Cre injection, we observe a significant accumulation of LAMP2-positive lysosomal vesicles specifically in GFP-Cre-positive, TH-positive dopaminergic neurons of the ipsilateral SN relative to the contralateral SN (Fig. 5a). LAMP2 vesicles also accumulate throughout the SN in non-dopaminergic cells. To quantify LAMP2 lysosomal pathology in general, we selectively identified large LAMP2-positive accumulations, based on fluorescence intensity and structure size, in the ipsilateral and contralateral SN. We find that ATP13A2 depletion following AAV-Cre delivery leads to a significant accumulation of large LAMP2-positive structures within cells throughout the ipsilateral SN (Fig. 5b). The number, average size and total area of these enlarged LAMP2-positive structures are increased in the ipsilateral versus contralateral SN (Fig. 5b). These data indicate lysosomal abnormalities in dopaminergic neurons and non-dopaminergic cells induced by ATP13A2 depletion in the SN.

Consistent with the phenotype of germline *ATP13A2* KO mice, we find a robust increase in the number and area of p62-positive inclusions specifically in the ipsilateral ventral midbrain of AAV-Cre-injected mice at 10 months (Fig. 6a). p62 is a critical autophagy substrate and adaptor protein that can be used as a reporter to monitor autophagy function, with the formation of p62-positive inclusions indicating autophagy and/or lysosomal disruption[28]. To evaluate lysosomal stress in response to ATP13A2 depletion, we examined the localization of Transcription Factor E3 (TFE3) in the ventral midbrain. Under normal conditions, TFE3

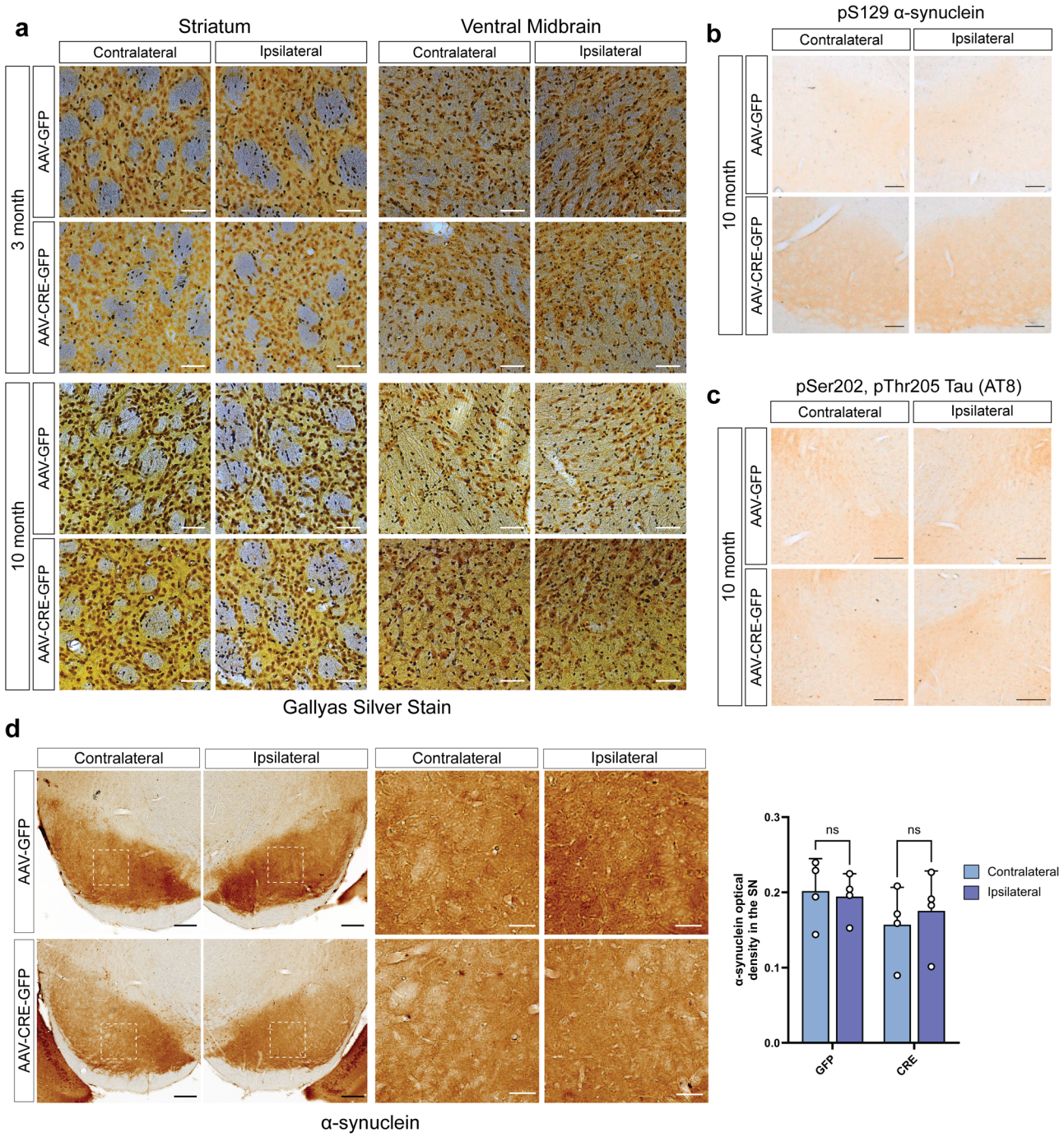

Fig. 4 | *ATP13A2* KO does not induce axonal damage or accumulation of protein aggregates. a Gallyas silver staining was used to detect axonal damage in AAV-Cre-GFP and AAV-GFP-injected *ATP13A2* floxed KO mice. Representative images of striatum and SN at 3 or 10 months after AAV injection. Scale bars: 50 µm. **b** SN sections from AAV-Cre-GFP or AAV-GFP mice immunostained for pSer129-α-synuclein at 10 months after injection. Scale bars: 100 µm. **c** SN sections from AAV-injected mice immunostained for pSer202/pThr205-Tau (AT8) at 10 months after injection. Scale bars: 200 µm. **d** Representative images of total α-synuclein immunostaining in the ventral midbrain (scale bars: 200 µm) or the SN (scale bars: 50 µm). Total α-synuclein optical density in the SN was measured using HALO analysis software. Bars represent mean ± SEM, $n = 4$ mice per group. *ns*, not significant.

localizes to lysosomal membranes. In response to starvation- or pharmacologically-induced lysosomal stress, TFE3 promotes lysosomal biogenesis by translocating to the nucleus and activating the transcription of a network of lysosomal genes[29]. At 3 months after AAV-Cre injection, we observe strong nuclear localization of TFE3 in a subset of Cre-GFP-positive cells in the ipsilateral SNpc and VTA (Fig. 6b). Immunostaining for TH indicates strong TFE3 nuclear localization in TH-negative neurons (Fig. 6b). TFE3 nuclear localization is not observed in the contralateral SN of AAV-Cre-injected mice, nor in either hemisphere of AAV-GFP-injected mice. Based on the high efficiency of *ATP13A2* knockout throughout the ventral midbrain induced by AAV-Cre, we anticipated more widespread lysosomal stress in this region at 3 months. Surprisingly, we only observe strong TFE3 nuclear localization in a small subset of cells. The timing of the TFE3 response to lysosomal stress in neurons in vivo has not been well characterized. Nuclear TFE3 could be a transient response to lysosomal stress in response to ATP13A2 depletion. Alternatively,

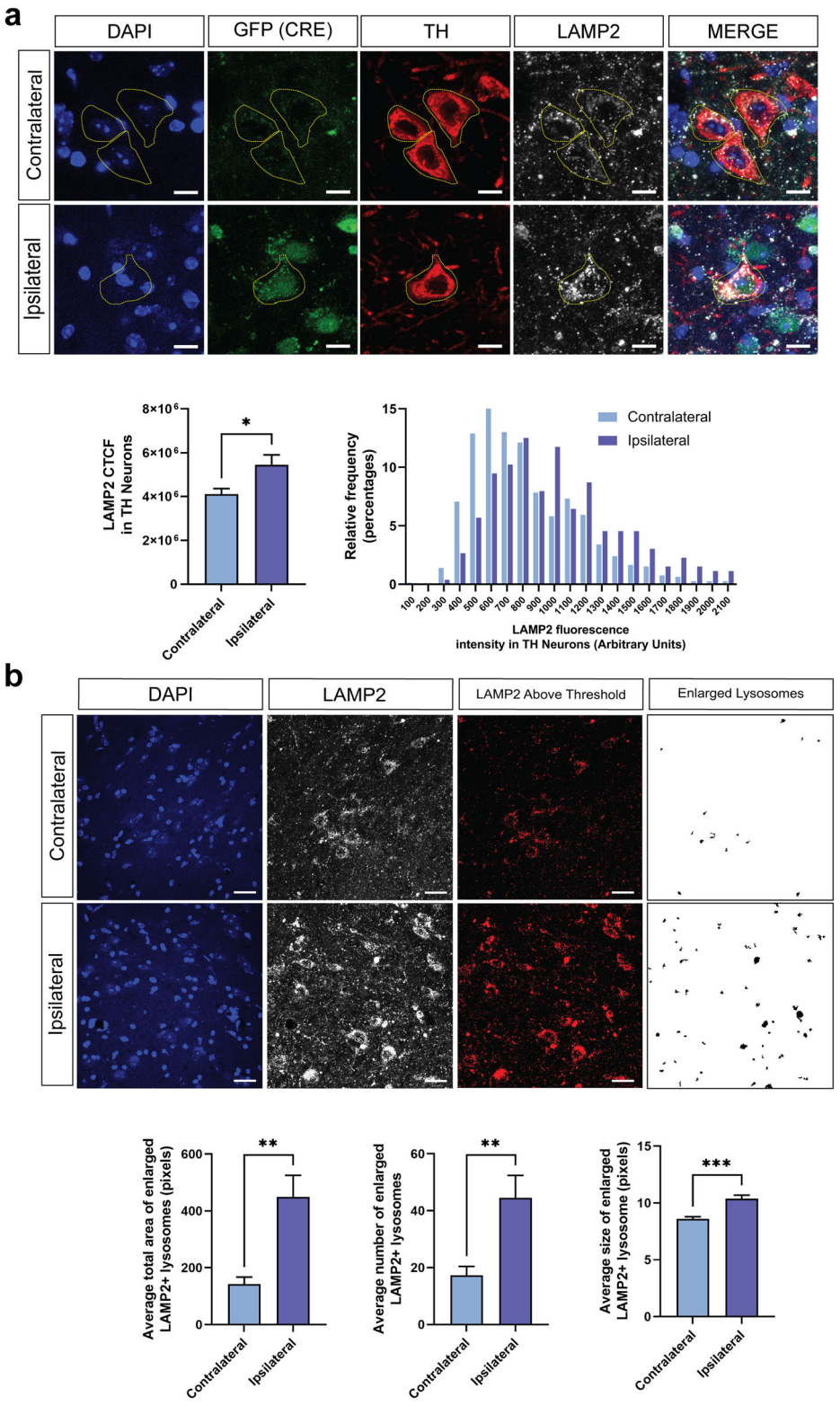

Fig. 5 | Loss of ATP13A2 leads to the accumulation of LAMP2-positive lysosomes in SNpc dopaminergic neurons and lysosomal swelling. a Confocal immunofluorescent images of LAMP2, TH and GFP (Cre) in the SN of *ATP13A2* floxed KO mice injected with AAV-Cre-GFP vector after 10 months. Scale bars: 10 µm. LAMP2-positive corrected total cell fluorescence (CTCF) intensity in TH-positive/Cre-GFP-positive cells in the ipsilateral SNpc versus TH-positive cells in the contralateral SNpc, was measured using NIS-Elements analysis software. (*Left graph*) Bars represent mean ± SEM, $n = 8$ mice per group. $^{*}P < 0.05$ by unpaired, Student's *t*-test. (*Right graph*) Frequency plot indicating the distribution of LAMP2-positive signal intensity in TH-positive neurons of the ipsilateral versus contralateral SNpc. Notice the overall rightward shift in frequency in the ipsilateral Cre-GFP-expressing neurons. **b** Immunofluorescent images of LAMP2 in the SNpc of *ATP13A2* floxed KO mice injected with AAV-Cre-GFP vector after 10 months. Scale bars: 25 µm. The LAMP2-positive signal brighter than an arbitrary threshold was analyzed using ImageJ software. Bright LAMP2-positive signal was further filtered to remove small LAMP2-positive structures to specifically identify enlarged/swollen lysosomes. The remaining LAMP2-positive lysosomal structures were subjected to a particle analysis to quantify the total area, number, or size. Bars represent mean ± SEM, $n = 8$ mice per group. $^{**}P < 0.01$ or $^{***}P < 0.001$ by unpaired, Student's *t*-test.

ATP13A2 depletion may cause a relatively mild form of lysosomal stress that does not consistently activate TFE3. Collectively, these data indicate that a subset of cells in the SN, including dopaminergic neurons, exhibit lysosomal activity deficits (p62 accumulation) and stress (nuclear TFE3) induced by the loss of ATP13A2.

To further evaluate changes in the autophagy-lysosome pathway induced by ATP13A2 loss, we quantified the steady-state levels of key lysosomal and autophagy proteins in soluble ventral midbrain extracts from mice injected with AAV-GFP or AAV-Cre after 3 or 6 months. Surprisingly, we do not find significant changes in the levels of lysosomal or autophagy proteins, including LAMP1, LAMP2, p62, cathepsin D species, LC3B-I and LC3B-II, ubiquitin, phospho-Thr73-Rab10 or phospho-Ser106-Rab12, in the ipsilateral ventral midbrain of AAV-Cre-injected mice at 3 months (Supplementary Fig. 5) or 6 months

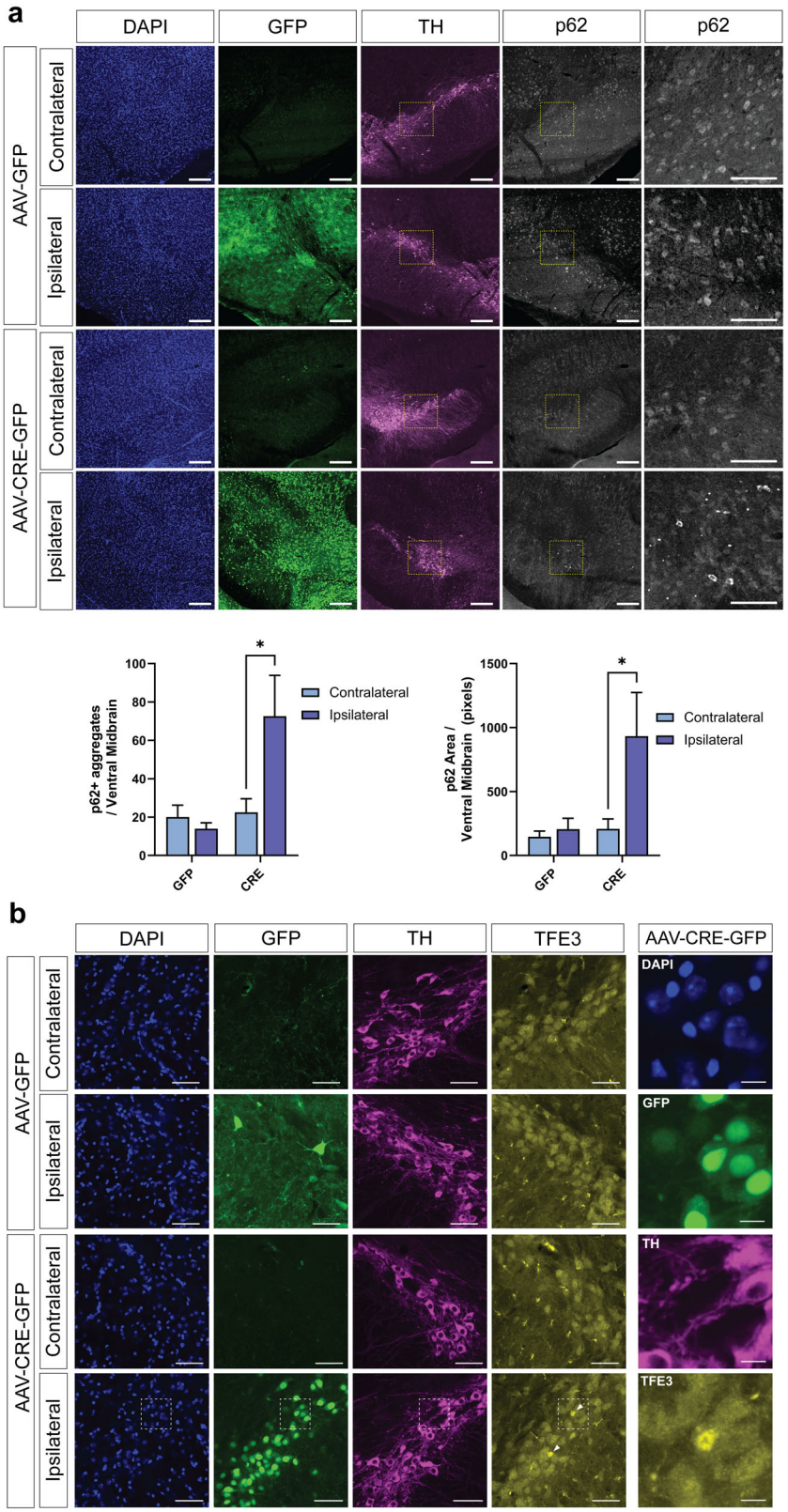

Fig. 6 | *ATP13A2* deletion disrupts autophagy and induces lysosomal stress. a Confocal immunofluorescent images of p62, TH and GFP in the ventral midbrain of *ATP13A2* floxed KO mice injected with AAV-Cre-GFP or AAV-GFP vectors after 10 months. Scale bars: 100 µm or 50 µm (zoom). p62-positive inclusion number (*left*) and area (*right*) in the ventral midbrain were measured using Cell Profiler image analysis software. Bars represent mean ± SEM, $n = 4$ mice per group. $^*P < 0.05$ by two-way ANOVA with Sidak's multiple comparisons test. **b** Confocal immunofluorescent images of TFE3, TH and GFP in the SN of *ATP13A2* floxed KO mice injected with AAV-Cre-GFP or AAV-GFP vectors after 3 months. Scale bars: 50 µm or 10 µm (zoom). Nuclear translocation of TFE3 (*arrowheads*) was only observed in the ipsilateral SN or VTA of AAV-Cre-GFP-injected mice. High magnification images of Cre-GFP-positive cells are shown from the boxed region, as indicated. Representative images from $n = 4$ mice per group.

(Supplementary Fig. 6). Rab10 and Rab12 are substrates of LRRK2 that can be phosphorylated in response to lysosomal stress or damage[30]. We also do not observe altered levels of total α-synuclein protein in these extracts, that can often accumulate with lysosomal impairment[31]. At 10 months following AAV-Cre injection, we do observe increased LAMP2 signal and p62 inclusions in numerous cells within the ipsilateral SN by confocal immunofluorescence (Figs. 5 and 6a). We suspect that 3 or 6 months after AAV-Cre injection is too early to detect bulk changes in lysosomal proteins in ventral midbrain extracts by Western blotting. Immunofluorescence would likely be more sensitive for detecting subtle changes in lysosomal proteins in individual cells at these timepoints, as we find at 10 months by immunostaining.

Discussion

The adult-onset KO of *ATP13A2* in the SN of mice induced by AAV-Cre delivery replicates many of the phenotypes initially observed in germline *ATP13A2* KO mice, including neuroinflammation and abnormalities in the endolysosomal pathway. Importantly, this approach additionally induces robust and progressive nigrostriatal pathway dopaminergic degeneration over a 10-month period, thereby recapitulating a major neuropathological hallmark of PD. Consistent with germline KO mice, however, the adult-onset deletion of *ATP13A2* does not induce the pathological aggregation of α-synuclein or tau.

The development of animal models that recreate the molecular pathology and progressive dopaminergic neurodegeneration that characterize PD is one of many critical steps in identifying and evaluating novel disease-modifying therapeutics. This new PD model targets one component of the endolysosomal pathway resulting in sustained lysosomal dysfunction in vivo, that induces neuroinflammation, autophagy dysfunction and eventual dopaminergic neuronal death. ATP13A2 depletion or loss-of-function mutations in *ATP13A2* also disrupt mitochondrial function in vitro, likely through impaired mitochondrial clearance[32,33]. Although mutations in *ATP13A2* are relatively rare in human PD subjects, lysosomal and mitochondrial dysfunction are observed or implicated in many forms of familial and sporadic PD. Accordingly, this adult-onset *ATP13A2* KO model may be useful in understanding both familial and sporadic forms of the disease as it provides a tool for evaluating putative therapeutic strategies targeting the endolysosomal pathway.

The development of dopaminergic neurodegeneration in this adult-onset, conditional *ATP13A2* KO model (Fig. 2) contrasts with the lack of neuronal loss in aged germline KO mice[24,25]. We suspect that germline KO mice may upregulate compensatory neuroprotective pathways that preserve dopaminergic neuronal viability, a mechanism that is likely not activated in the adult brain upon conditional *ATP13A2* deletion. A similar phenomenon is observed in *parkin* KO mice, where the Cre-mediated, adult-onset KO of *parkin* is sufficient to induce progressive neurodegeneration whereas germline KO mice consistently fail to do so with advanced age[34–36]. One study has further shown that the lack of neurodegeneration in germline *parkin* KO mice may relate to the upregulation of the mitochondrial pro-survival factor, Mcl-1, and reducing *Mcl-1* gene dosage is sufficient to sensitize *parkin* KO mice to dopaminergic neuronal loss and motor deficits[37,38]. Similar compensatory pathways may be upregulated in germline *ATP13A2* KO mice that mask neurodegeneration, such as lysosomal stress or damage genes, and this would be important to explore in future studies. Newer techniques such as single-nucleus RNA-sequencing of ventral midbrain tissue would permit a comprehensive analysis of both models and provide insight into neuronal susceptibility and specific adaptations to ATP13A2 depletion.

In the *ATP13A2* floxed KO mice, we do observe the nuclear translocation of TFE3 in a small subset of cells in the SN (Fig. 6B), and this may be sufficient to preserve viability in these cells. It is possible that dopaminergic neurons that eventually degenerate in this KO model are not able to mount an effective response to lysosomal damage by activating the Coordinated Lysosomal Expression and Regulation (CLEAR) gene network via the transcription factors TFE3 or TFEB[39]. The lack of evidence for α-synuclein and tau aggregation in the conditional *ATP13A2* KO mice (Fig. 4b–d) is consistent with human neuropathology data from a single *ATP13A2*-linked KRS patient[27] as well as germline *ATP13A2* KO mice[24]. More importantly, the development of key phenotypes in germline KO mice, such as reactive gliosis, lipofuscinosis, ubiquitinated protein aggregates, and endolysosomal abnormalities, were shown to occur even in the absence of α-synuclein[24]. A similar study in a rat viral-based model of PD revealed that ATP13A2 overexpression was unable to protect against dopaminergic neuronal loss and motor deficits induced by the expression of human wild-type α-synuclein[22]. These data suggest that α-synuclein aggregation may not be a key part of the disease spectrum induced by loss-of-function *ATP13A2* mutations.

The recent characterization of ATP13A2 as a lysosomal polyamine exporter protein suggests that adult-onset *ATP13A2* KO may disrupt polyamine homeostasis in the ventral midbrain[15]. Measuring polyamine levels in ventral midbrain tissue when ATP13A2 is depleted will provide an important confirmation of this activity and insight into this pathway. Additionally, altering polyamine levels in the brain may be sufficient to modulate the pathogenic effects of adult-onset *ATP13A2* KO in nigral dopaminergic neurons. For example, treatment with difluoromethylornithine (DFMO) to inhibit ornithine decarboxylase 1 (ODC1), the rate-limiting enzyme required for polyamine synthesis, would systemically reduce putrescine and spermidine levels in mice[40,41]. Increasing polyamine levels in the brain is more challenging. Dietary supplementation of polyamines can increase circulating polyamine levels, but polyamines are not known to efficiently cross the blood brain barrier[42,43]. Since high levels of polyamines cause toxicity in primary neuronal cultures, injecting concentrated polyamines directly into the brain would likely induce toxicity in mice, and may not be a viable experimental strategy[15]. Future studies investigating the effects of altering polyamine levels in the brain of adult-onset *ATP13A2* KO mice could illuminate important aspects of the role of ATP13A2 in polyamine homeostasis in vivo and the effects of modulating polyamine levels on endolysosomal pathway-mediated neurotoxicity.

Methods

Animals

Male and female homozygous *ATP13A2 lox*P-flanked (floxed) KO mice (*RRID:IMSR_JAX:028387*), containing floxed exons 2-3 (Fig. 1a), were originally described by Kett et al. [24] and obtained from The Jackson Laboratory[24]. *ATP13A2* floxed KO alleles were genotyped by PCR with genomic DNA[24]. Male and female homozygous ROSA26-LRRK2^{R1441C} mice (*RRID:IMSR_JAX:026293*) containing a floxed STOP cassette upstream of a human R1441C LRRK2 transgene were also used for this study. Mice were housed in a pathogen-free barrier facility with a 12-h light/dark cycle. Food and water were provided *ad libitum*. Mice were treated in accordance with the NIH Guidelines for the Care and Use of Laboratory Animals. All animal experiments were approved by the Van Andel Institute Animal Care and Use Committee (IACUC).

Stereotactic brain surgery

Homozygous *ATP13A2* floxed KO mice (age 2-6 months) were anesthetized using 2% isoflurane and positioned in stereotactic frames. We used the following coordinates to administer unilateral injections of AAV vectors into the SNpc: anterior-posterior (A-P), -2.9 mm; medio-lateral (M-L), -1.3 mm; dorso-ventral (D-V), -4.2 mm. AAV vectors (2 µl volume) were delivered at a flow rate of 0.2 µl/min. AAV vectors were purchased from University of North Carolina (UNC) Vector Core. Mice received ~1.12 $\times 10^{10}$ viral genomes (vg) of AAV2/5-CMV-Cre-GFP (Lot# AV4955D) or ~1.16 $\times 10^{10}$ vg of AAV2/5-CMV-GFP (Lot# AV5617B) as a control. Mice were sacrificed at 3, 6 or 10 months after AAV injection. Homozygous ROSA26-LRRK2^{R1441C} mice were unilaterally injected with ~1.0 $\times 10^{10}$ vg of AAV2/5-CMV-Cre-GFP into the SNpc and sacrificed after 12 months for histological analysis. For protocol see: https://doi.org/10.17504/protocols.io.81wgbx373lpk/v1.

BaseScope™ in situ hybridization

BaseScope RNA In Situ Hybridization was performed following the manufacturer's instructions (ACD Bio) using a custom probe designed to recognize exons 2-3 of mouse ATP13A2 (1230491-C1). BaseScope™ images were obtained using Zeiss Axioscan 7 Microscope Slide Scanner at 20X magnification at a resolution of 0.173 µm/pixel. BaseScope™ signal area was measured in the SN using HALO analysis software (Area quantification module; Indica Labs Inc.) (RRID:SCR_018350). Refer to Table S1 for imaging acquisition details. 1 or 2 brain sections were analyzed per mouse. For protocol see: https://doi.org/10.17504/protocols.io.5qpvo364zv4o/v1. Tyrosine hydroxylase (TH) labeling with BaseScope™ in situ hybridization was performed after BaseScope™ in situ hybridization using ImmPRESS

alkaline phosphatase immunolabeling (Vector Labs) following manufacturer instructions. For protocol see: https://doi.org/10.17504/protocols.io.kqdg325rzv25/v1.

Genomic PCR

Genomic DNA was isolated from the ipsilateral and contralateral ventral midbrain hemispheres at 3 months after AAV-GFP or AAV-Cre-GFP injections using the DNeasy Blood and Tissue kit (Qiagen) following the manufacturer's instructions. Genomic PCR for *ATP13A2* floxed or KO alleles was performed using 100 ng genomic DNA and the Kapa2g Fast HotStart PCR Kit (Roche). PCR primers included a forward primer (5′-CTGCAGCTTCGAGAGGAAAG-3′), one floxed reverse primer (5′-CACTCTGTCCTCAGGCTTTC-3′), and one KO reverse primer (5′-AGGTGGGAATCGGGCTAGAG-3′). For protocol see: https://doi.org/10.17504/protocols.io.kqdg324zzv25/v1.

Immunohistochemistry

Mice were deeply anesthetized followed by transcardial perfusion with 0.9% NaCl and then 4% paraformaldehyde (PFA) in 0.1 M phosphate buffer (PB) at pH 7.4. After perfusion, whole brains were removed and incubated in 4% PFA in 0.1 M PB at 4 °C overnight. Brain tissue was cryoprotected using 30% sucrose in 0.1 M PB for ≥ 24 hours before microtome sectioning at 35 µm thickness. Immunohistochemical staining using primary antibodies, biotinylated anti-IgG secondary antibodies (Vector Labs), Vectastain Elite ABC kit (Vector Labs), and 3,3′-diaminobenzidine (DAB; Vector Labs) was performed as described by Dues et al. [44]. Midbrain sections immunostained for TH were incubated in cresyl violet solution for 15 minutes. Primary antibodies used include TH (N300-109; Novus Biological), Iba1 (019-19741; Fujifilm Wako Chemical USA), GFAP (G3893; Millipore Sigma), pS129-α-synuclein (ab51253; Abcam), pSer202/pThr205-Tau (AT8) (MN1020; Thermofisher) and GFP (A-11122; Thermofisher). Secondary antibodies include biotinylated goat-anti rabbit and goat-anti mouse (Vector labs). Refer to Supplementary Table 2 for antibody details and dilutions used. For protocols see: https://doi.org/10.17504/protocols.io.5jyl8pzk9g2w/v1 and https://doi.org/10.17504/protocols.io.3byl497zjgo5/v1.

For immunofluorescence, brain sections were incubated in primary antibody at 4 °C overnight and then in secondary antibody (1:500) conjugated to the appropriate fluorophore for 2 hours. Primary antibodies include TH (N300-109; Novus Biological or ab76442; Abcam), LAMP2 (ab13524; Abcam), p62 (GP62-C; Progen), GFP (A-11122; Thermofisher or 11814460001; Roche or GFP-1010; Aves Labs), GAD67 (MAB5406; Millipore Sigma), parvalbumin (ab11427; Abcam) and TFE3 (ab93808; Abcam). Secondary antibodies were purchased from Thermofisher Scientific. They include: goat-anti rabbit AlexaFluor-488 (A-11008), goat-anti rabbit AlexaFluor-546 (A-11010), goat-anti rabbit AlexaFluor-647 (A-21245), goat-anti mouse AlexaFluor-488 (A-11029), goat-anti mouse AlexaFluor-546 (A-11003), goat-anti rat AlexaFluor-647 (A-21247), goat-anti chicken AlexaFluor-488 (A-11039), and goat-anti chicken AlexaFluor-647 (A-21449). Refer to Supplementary Table 2 for antibody details and dilutions used. For protocol see: https://doi.org/10.17504/protocols.io.bp2l62nk1gqe/v1.

Optical density analysis of striatal TH-positive terminals

DAB immunostaining was used to label TH in coronal brain sections containing the striatum. Images were obtained using an Aperio ScanScope XT slide scanner at 20X magnification at a resolution of 0.5 µm/pixel. Mean optical density in the striatum was measured in every 4th section using HALO analysis software (Area quantification module; Indica Labs Inc., RRID:SCR_018350). Refer to Supplementary Table 1 for imaging acquisition details. 6-8 sections were analyzed per mouse.

Stereological quantification of substantia nigra TH-positive neurons

TH neuronal loss and Nissl loss in the SNpc were estimated using unbiased stereological quantification of TH+ and Nissl+ neurons. For this purpose, we analyzed every 4th serial section of the ventral midbrain using the optical fractionator probe of the StereoInvestigator software (MicroBrightField Biosciences, RRID:SCR_018948). Refer to Supplementary Table 1 for imaging acquisition details. Tissue was immunostained for TH and counterstained with 0.1% cresyl violet. Analysis area covered the entire SNpc. Random, systematic sampling was performed using a grid of 120 × 120 µm squares and applying an optical dissector with the dimensions 50 × 50 × 14 µm. During analysis, investigators were blinded to experimental conditions.

Microglia analysis

DAB immunostaining was used to label Iba1 in coronal midbrain sections. Images were obtained using an Aperio ScanScope XT slide scanner at 20X magnification at a resolution of 0.5 µm/pixel. Iba1-positive area, microglial number and microglia cell body size were measured in the SN using HALO analysis software (Area quantification module or Microglia activation module; Indica Labs Inc., RRID:SCR_018350). Refer to Supplementary Table 1 for imaging acquisition details. 1 or 2 sections were analyzed per mouse.

GFAP analysis

DAB immunostaining was used to label GFAP in coronal midbrain sections. Images were obtained using an Aperio ScanScope XT slide scanner at 20X magnification at a resolution of 0.5 µm/pixel. GFAP-positive area was measured in the SN using HALO analysis software (Area quantification module, Indica Labs Inc., RRID:SCR_018350). Refer to Supplementary Table 1 for imaging acquisition details. 2 sections were analyzed per mouse.

Gallyas silver staining

Gallyas silver staining was performed using the FD NeuroSilver™ Kit II (FD NeuroTechnologies Inc) according to the manufacturer's instructions. For protocol see: https://doi.org/10.17504/protocols.io.5qpvo366zv4o/v1.

Optical density analysis of total α-synuclein

DAB immunostaining was used to label total α-synuclein in coronal midbrain sections. Images were obtained using an Aperio ScanScope XT slide scanner at 20X magnification at a resolution of 0.5 µm/pixel. Mean optical density in the SN was measured using HALO analysis software (Area quantification module; Indica Labs Inc.) (RRID:SCR_018350). Refer to Supplementary Table 1 for imaging acquisition details. 2 sections were analyzed per mouse in 4 mice per group.

LAMP2 analysis

Immunofluorescence was used to label LAMP2, TH and Cre-GFP in coronal midbrain sections. Z-stack images were obtained using a Nikon A1plus-RSi Laser-Scanning Confocal microscope with a 100X objective at a resolution of 0.205 µm/pixel. Max intensity projection images were deconvolved using Huygens Professional (Scientific Volume Imaging) deconvolution software. LAMP2 corrected total cellular fluorescence (CTCF) intensity was measured in TH + /Cre-GFP+ neurons in the SNpc using NIS-Elements analysis software (Nikon, RRID: SCR_002776). Refer to Supplementary Table 1 for imaging acquisition details. 19-43 TH + /Cre-GFP+ neurons were analyzed per ipsilateral SNpc per mouse. 78-153 TH+ neurons were analyzed per contralateral SNpc per mouse. Average LAMP2 CTCF for each mouse was used for analysis.

The same images were used to analyze enlarged LAMP2+ structures in the SNpc using NIH ImageJ (FIJI) (RRID:SCR_003070). Refer to Supplementary Table 1 for imaging acquisition details. To capture the brightest LAMP2+ structures, image thresholds were adjusted to 2908, 65535. Particles smaller than 200 pixels were removed before running a particle analysis to assess the enlarged LAMP2+ structures. Number, average size and total area of LAMP2+ structures were recorded. Data is shown as the average for each measurement per image per mouse.

Parvalbumin and GAD67 analysis

Immunofluorescence was used to label parvalbumin, GAD67 and GFP or Cre-GFP in coronal midbrain sections. Z-stack images were obtained using an ImageXpress Confocal HT Microscope with a 20X objective at a resolution of 0.3411 µm/pixel. 2-dimensional max intensity projection images were used for analysis. GAD67 mean fluorescence intensity was measured using Cell Profiler (v4.2.5) (RRID:SCR_007358) in the SN. Refer to Supplementary Table 1 for imaging acquisition details. 1-3 brain sections were analyzed per mouse. Data are shown as average fluorescence intensity per section per mouse. Parvalbumin neurons were counted in the SN using Cell Profiler (v4.2.5) (RRID:SCR_007358). 1-3 brain sections were analyzed per mouse. Data are shown as average parvalbumin neuron count per section per mouse.

p62 analysis

Immunofluorescence was used to label p62, TH and GFP or Cre-GFP in coronal midbrain sections. Z-stack images were obtained using a Nikon A1plus-RSi Laser-Scanning Confocal microscope with a 10X objective at a resolution of 0.610 µm/pixel. Max intensity projections were used for analysis. Bright p62-positive inclusions were identified in SN using Cell Profiler (v4.2.5) (RRID:SCR_007358). Refer to Supplementary Table 1 for imaging acquisition details. 2-3 brain sections were analyzed per mouse in 4 mice per group. Number of p62-positive inclusions and total area occupied by p62-positive inclusions was measured per SN section per mouse.

Western blot analysis

Ventral midbrain tissue was homogenized and lysed as described by Mir et al. [45] for analysis of phosophorylated Rab proteins[45]. (For protocol see: https://doi.org/10.17504/protocols.io.261ge545jg47/v1). Ice-cold RIPA buffer (150 mM NaCl, 50 mM Tris pH 8.5, 1% nonidet P-40, 0.05% sodium deoxycholate, 0.1% SDS) was added to Triton-insoluble pellets and sonicated at 10% amplitude for 15 seconds. Lysates were then centrifuged at 6000 rcf for 10 minutes at 4 °C. Protein concentrations were measured in Triton-soluble fractions and in RIPA-soluble fractions using a Pierce BCA protein assay following the manufacturer's instructions (Thermofisher Scientific).

Lysates were mixed with 5X Laemmli sample buffer and incubated at 70 °C for 10 minutes. 40-75 µg of protein was resolved on 12.5% or 15% SDS-polyacrylamide gels. Protein was transferred to 0.2 µm nitrocellulose membranes (Amersham) at 20 V overnight. Membranes were blocked in 5% nonfat milk in TBST (20 mM Tris pH 7.5, 150 mM NaCl, 0.1% Tween-20) for 1 h and then incubated in primary antibody in blocking buffer at 4 °C overnight. Prior to imaging, membranes were washed and incubated with HRP-conjugated secondary antibodies (Jackson Immunoresearch) and developed using enhanced chemiluminescence (ECL) or ECL prime (Amersham). Membranes were stripped 2-3 times between primary antibodies, using Restore WesternBlot Stripping Buffer (Thermofisher Scientific) according to manufacturer's instructions. Images were acquired using an Amersham Imager 680 imager and were analyzed using NIH ImageJ (FIJI; v2.14.0).

Primary antibodies used for Western blotting include GFP (11814460001; Roche), pThr73-Rab10 (ab230261; Abcam), total Rab10 (8127 S; Cell Signaling Technology), pSer106-Rab12 (ab256487; Abcam), total Rab12 (18843-1-AP; Protein Tech), α-synuclein (610787; BD Biosciences), actin (MAB1501, Millipore), LAMP1 (ab24170; Abcam), LAMP2 (ab13524; Abcam), p62 (GP62-C; Progen), cathepsin D (sc-6487-R; Santa Cruz), LC3b (3868; Cell Signaling Technology), ubiquitin (3936; Cell Signaling Technology) and Dynamin-1 (PA1-660; Thermofisher Scientific). Refer to Supplementary Table 2 for antibody details and dilutions used.

Statistical analysis

Data was analyzed with GraphPad Prism 10 (v10.2.2) (RRID:SCR_002798) software by unpaired Student's *t*-test, paired Student's *t*-test or two-way ANOVA with Sidak's multiple comparisons test. Graphs were generated using GraphPad Prism 10 and depict all data as mean ± SEM.

Data availability

All data generated and analyzed in this study has been presented in this manuscript. The datasets generated for this study are available at zenodo.org/records/11068570.

Received: 25 January 2024; Accepted: 4 July 2024;
Published online: 20 July 2024

References

1. Lesage, S. & Brice, A. Parkinson's disease: from monogenic forms to genetic susceptibility factors. *Hum. Mol. Genet* **18**, R48–R59 (2009).
2. Deng, H., Wang, P. & Jankovic, J. The genetics of Parkinson disease. *Ageing Res Rev.* **42**, 72–85 (2018).
3. Blauwendraat, C., Nalls, M. A. & Singleton, A. B. The genetic architecture of Parkinson's disease. *Lancet Neurol.* **19**, 170–178 (2020).
4. Smolders, S. & Van Broeckhoven, C. Genetic perspective on the synergistic connection between vesicular transport, lysosomal and mitochondrial pathways associated with Parkinson's disease pathogenesis. *Acta Neuropathol. Commun.* **8**, 63 (2020).
5. Abeliovich, A. & Gitler, A. D. Defects in trafficking bridge Parkinson's disease pathology and genetics. *Nature* **539**, 207–216 (2016).
6. Santoro, L. et al. Novel ATP13A2 (PARK9) homozygous mutation in a family with marked phenotype variability. *Neurogenetics* **12**, 33–39 (2011).
7. Di Fonzo, A. et al. ATP13A2 missense mutations in juvenile parkinsonism and young onset Parkinson disease. *Neurology* **68**, 1557–1562 (2007).
8. Lin, C. H. et al. Novel ATP13A2 variant associated with Parkinson disease in Taiwan and Singapore. *Neurology* **71**, 1727–1732 (2008).
9. Ramirez, A. et al. Hereditary parkinsonism with dementia is caused by mutations in ATP13A2, encoding a lysosomal type 5 P-type ATPase. *Nat. Genet* **38**, 1184–1191 (2006).
10. Ning, Y. P. et al. PARK9-linked parkinsonism in eastern Asia: mutation detection in ATP13A2 and clinical phenotype. *Neurology* **70**, 1491–1493 (2008).
11. Estrada-Cuzcano, A. et al. Loss-of-function mutations in the ATP13A2/PARK9 gene cause complicated hereditary spastic paraplegia (SPG78). *Brain* **140**, 287–305 (2017).
12. Spataro, R. et al. Mutations in ATP13A2 (PARK9) are associated with an amyotrophic lateral sclerosis-like phenotype, implicating this locus in further phenotypic expansion. *Hum. Genomics* **13**, 19 (2019).
13. Kruer, M. C. et al. Analysis of ATP13A2 in large neurodegeneration with brain iron accumulation (NBIA) and dystonia-parkinsonism cohorts. *Neurosci. Lett.* **523**, 35–38 (2012).
14. Bras, J., Verloes, A., Schneider, S. A., Mole, S. E. & Guerreiro, R. J. Mutation of the parkinsonism gene ATP13A2 causes neuronal ceroid-lipofuscinosis. *Hum. Mol. Genet* **21**, 2646–2650 (2012).
15. van Veen, S. et al. ATP13A2 deficiency disrupts lysosomal polyamine export. *Nature* **578**, 419–424 (2020).
16. Sim, S. I., von Bulow, S., Hummer, G. & Park, E. Structural basis of polyamine transport by human ATP13A2 (PARK9). *Mol. Cell* **81**, 4635–4649.e4638 (2021).
17. Chen, X. et al. Cryo-EM structures and transport mechanism of human P5B type ATPase ATP13A2. *Cell Discov.* **7**, 106 (2021).
18. Ramonet, D. et al. PARK9-associated ATP13A2 localizes to intracellular acidic vesicles and regulates cation homeostasis and neuronal integrity. *Hum. Mol. Genet* **21**, 1725–1743 (2012).
19. Podhajska, A. et al. Common pathogenic effects of missense mutations in the P-type ATPase ATP13A2 (PARK9) associated with early-onset parkinsonism. *PLoS One* **7**, e39942 (2012).
20. Dehay, B. et al. Loss of P-type ATPase ATP13A2/PARK9 function induces general lysosomal deficiency and leads to Parkinson disease neurodegeneration. *Proc. Natl Acad. Sci. USA* **109**, 9611–9616 (2012).

21. Usenovic, M., Tresse, E., Mazzulli, J. R., Taylor, J. P. & Krainc, D. Deficiency of ATP13A2 leads to lysosomal dysfunction, alpha-synuclein accumulation, and neurotoxicity. *J. Neurosci.* **32**, 4240–4246 (2012).
22. Daniel, G. et al. alpha-Synuclein-induced dopaminergic neurodegeneration in a rat model of Parkinson's disease occurs independent of ATP13A2 (PARK9). *Neurobiol. Dis.* **73**, 229–243 (2015).
23. Murphy, K. E., Cottle, L., Gysbers, A. M., Cooper, A. A. & Halliday, G. M. ATP13A2 (PARK9) protein levels are reduced in brain tissue of cases with Lewy bodies. *Acta Neuropathol. Commun.* **1**, 11 (2013).
24. Kett, L. R. et al. alpha-Synuclein-independent histopathological and motor deficits in mice lacking the endolysosomal Parkinsonism protein Atp13a2. *J. Neurosci.* **35**, 5724–5742 (2015).
25. Schultheis, P. J. et al. Atp13a2-deficient mice exhibit neuronal ceroid lipofuscinosis, limited alpha-synuclein accumulation and age-dependent sensorimotor deficits. *Hum. Mol. Genet* **22**, 2067–2082 (2013).
26. Tsika, E. et al. Conditional expression of Parkinson's disease-related R1441C LRRK2 in midbrain dopaminergic neurons of mice causes nuclear abnormalities without neurodegeneration. *Neurobiol. Dis.* **71**, 345–358 (2014).
27. Chien, H. F. et al. Neuropathologic Findings in a Patient With Juvenile-Onset Levodopa-Responsive Parkinsonism Due to ATP13A2 Mutation. *Neurology* **97**, 763–766 (2021).
28. Klionsky, D. J. et al. Guidelines for the use and interpretation of assays for monitoring autophagy (4th edition). *Autophagy* **17**, 1–382 (2021).
29. Martina, J. A. et al. The Nutrient-Responsive Transcription Factor TFE3 Promotes Autophagy, Lysosomal Biogenesis, and Clearance of Cellular Debris. *Sci. Signal.* **7**, ra9 (2014).
30. Wang, X. et al. Rab12 is a regulator of LRRK2 and its activation by damaged lysosomes. *eLife* **12**. https://doi.org/10.7554/eLife.87255 (2023).
31. Zhu, X., Prakash, S. S., McAuliffe, G. & Pan, P. Y. Synaptojanin1 Modifies Endolysosomal Parameters in Cultured Ventral Midbrain Neurons. *eNeuro* **10**. https://doi.org/10.1523/eneuro.0426-22.2023 (2023).
32. Gusdon, A. M., Zhu, J., Van Houten, B. & Chu, C. T. ATP13A2 regulates mitochondrial bioenergetics through macroautophagy. *Neurobiol. Dis.* **45**, 962–972 (2012).
33. Grünewald, A. et al. ATP13A2 mutations impair mitochondrial function in fibroblasts from patients with Kufor-Rakeb syndrome. *Neurobiol. Aging* **33**, 1843.e1841–1847 (2012).
34. Shin, J. H. et al. PARIS (ZNF746) repression of PGC-1α contributes to neurodegeneration in Parkinson's disease. *Cell* **144**, 689–702 (2011).
35. Von Coelln, R. et al. Loss of locus coeruleus neurons and reduced startle in parkin null mice. *Proc. Natl Acad. Sci. USA* **101**, 10744–10749 (2004).
36. Goldberg, M. S. et al. Parkin-deficient mice exhibit nigrostriatal deficits but not loss of dopaminergic neurons. *J. Biol. Chem.* **278**, 43628–43635 (2003).
37. Ekholm-Reed, S., Goldberg, M. S., Schlossmacher, M. G. & Reed, S. I. Parkin-dependent degradation of the F-box protein Fbw7β promotes neuronal survival in response to oxidative stress by stabilizing Mcl-1. *Mol. Cell. Biol.* **33**, 3627–3643 (2013).
38. Ekholm-Reed, S. et al. Reducing Mcl-1 gene dosage induces dopaminergic neuronal loss and motor impairments in Park2 knockout mice. *Commun. Biol.* **2**, 125 (2019).
39. Sardiello, M. et al. A gene network regulating lysosomal biogenesis and function. *Sci. (N. Y., N. Y.)* **325**, 473–477 (2009).
40. Najm, I., Vanderklish, P., Lynch, G. & Baudry, M. Effect of treatment with difluoromethylornithine on polyamine and spectrin breakdown levels in neonatal rat brain. *Dev. Brain Res.* **63**, 287–289 (1991).
41. Malaterre, J. et al. A novel role for polyamines in adult neurogenesis in rodent brain. *Eur. J. Neurosci.* **20**, 317–330 (2004).
42. Soda, K., Dobashi, Y., Kano, Y., Tsujinaka, S. & Konishi, F. Polyamine-rich food decreases age-associated pathology and mortality in aged mice. *Exp. Gerontol.* **44**, 727–732 (2009).
43. Shin, W. W., Fong, W. F., Pang, S. F. & Wong, P. Limited blood-brain barrier transport of polyamines. *J. neurochemistry* **44**, 1056–1059 (1985).
44. Dues, D. J., Nguyen, A. P. T., Becker, K., Ma, J. & Moore, D. J. Hippocampal subfield vulnerability to alpha-synuclein pathology precedes neurodegeneration and cognitive dysfunction. *NPJ Parkinson's disease* **9**. https://doi.org/10.1038/s41531-023-00574-1 (2023).
45. Mir, R. et al. The Parkinson's disease VPS35[D620N] mutation enhances LRRK2-mediated Rab protein phosphorylation in mouse and human. *Biochem J.* **475**, 1861–1883 (2018).

Acknowledgements

We would like to thank the outstanding core facilities at the Van Andel Institute that supported this work, including the Vivarium Core, the Pathology and Biorepository Core and the Optical Imaging Core. Figure 1a, b is made using BioRender. The study is funded by the joint efforts of The Michael J. Fox Foundation for Parkinson's Research (MJFF) and the Aligning Science Across Parkinson's (ASAP) initiative. MJFF administers the grant (ASAP-000592, to D.J.M.) on behalf of ASAP and itself. We are also grateful for funding support from a Parkinson's Foundation post-doctoral fellowship (PF-FBS-1894, to M.L.E.) and the Van Andel Institute.

Author contributions

M.L.E. designed, performed, and analyzed most experiments. K.S. assisted with immunohistochemistry and immunofluorescence experiments. N.L. performed stereotactic surgery, immunohistochemistry and analyzed experiments using ROSA26-LRRK2^{R1441C} mice. N.L. and X.C. assisted with stereotactic surgeries. D.J.M. conceptualized and supervised this research. M.L.E. and D.J.M. wrote the manuscript.

Competing interests

The authors declare no competing interests.

Additional information

Supplementary information The online version contains supplementary material available at https://doi.org/10.1038/s41531-024-00748-5.

Correspondence and requests for materials should be addressed to Darren J. Moore.